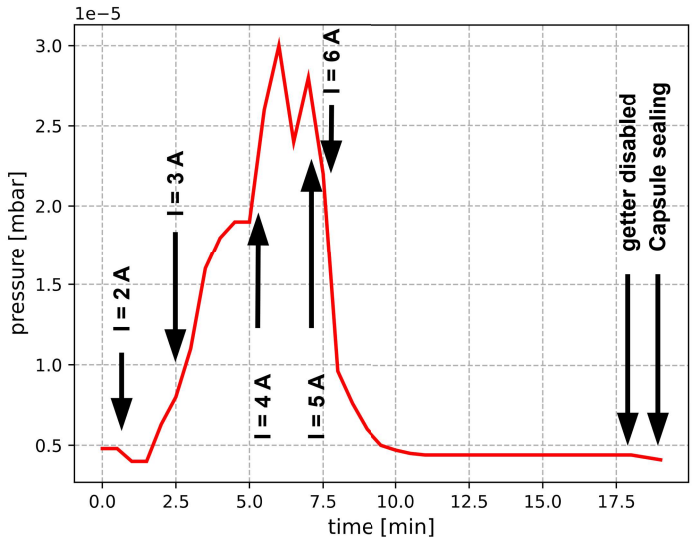

Figure 2.14: Capsule pressure profile during getter activation

experimental configuration is much more favorable, as the reduced pressure gradient between the inside and outside of the capsule helps maintain the internal vacuum level, while cryogenic conditions further improve it [28]. Consequently, much longer operational time window for our detectors should be expected.

To progress this work, the next step will involve the development of a hot cathode to be integrated into the capsule, enabling more accurate in situ pressure monitoring. Unfortunately, preliminary investigations indicate that commercially available devices of sufficiently small size and capable of measuring such low pressures are currently not available. The results obtained may eventually allow for an evaluation of the replacement of the currently adopted Helicoflex® gaskets with Helicoflex® Delta gaskets, which would provide superior sealing performance under equivalent tightening conditions. Finally, it will be necessary to repeat these tests with the capsule at cryogenic temperature.

2.6 Detector Support Structure

Within the capsule, the detector is held by a carefully designed mechanical support system, which ensures both structural stability and functionality.

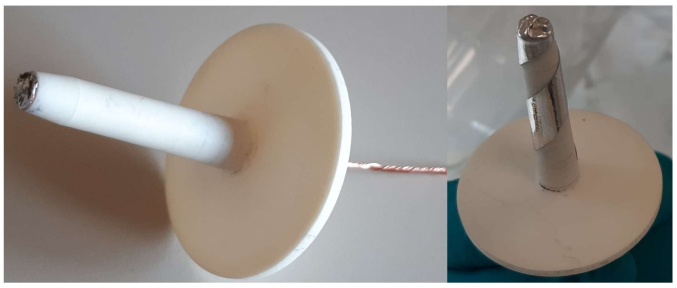

Figure 2.15: Photograph of the alumina cone that supports the HPGe crystal and houses the high-voltage rod. A thin indium layer is used at the interface with the inner electrode to prevent mechanical friction.

Figure 2.16: Photograph of the copper clamp used for the high-voltage connection.

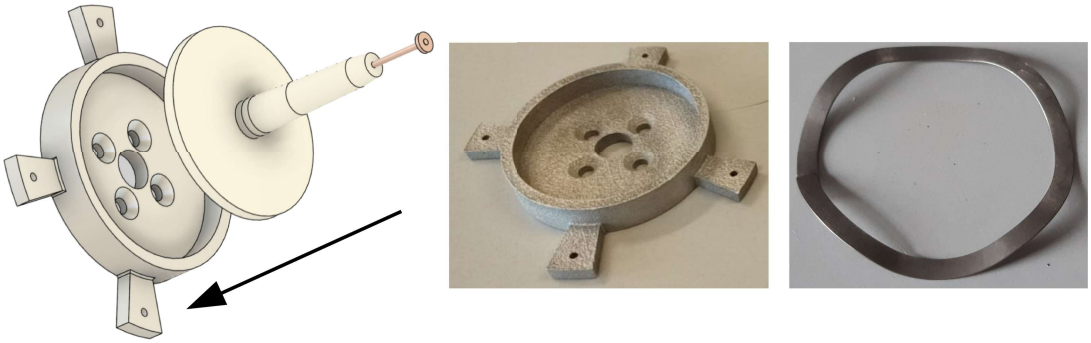

Figure 2.17: 3D rendering of the assembly of the cone supporting the detector, and photograph of the aluminum holder that supports the cone via the single-wave spring reported on the right.

The HPGe crystal is supported by a hollow conical body made of alumina, as illustrated in Fig. 2.15. It fits together the inner electrode by means of a protective indium layer, introduced to avoid any mechanical friction with the electrode itself. Inside the cone an electric rod is placed. It is used to apply the high-negative voltage ($3\,\mathrm{kV} - 5\,\mathrm{kV}$) needed for the detector polarization. This component is connected to the flange rod (Fig. 2.3) through the clamp shown in Fig. 2.16. A PTFE ring was also added around the clamp to ensure electrical insulation from the surrounding structure.

The base of the cone is located on a stainless steel single-wave annular spring, placed inside an aluminum spring-holder, directly screwed to the flange (see Fig. 2.17). The spring is made of Inconel, a nickel-based super-alloy characterized by excellent corrosion resistance and high strength, which retains its elastic properties at liquid-nitrogen temperatures. The system made by detector, cone, spring and spring-holder is closed by a PEEK (PoliEther-Ether-Ketone) cylindrical case to firmly keep the crystal in position independently from the container absolute orientation. The complete assembly is reported in Fig. 2.18.

An aluminum ring enables the PEEK case to be fastened to the spring-holder with four M2.5 steel screws. Careful control of the screw tightening is required, as overcompression may lead to permanent degradation of the crystal. Based on several experimental tests, we determined that applying a tightening force equal to twice the weight of the crystal is appropriate, as this value ensures reliable and stable positioning. Considering a detector with a mass of $600\,\mathrm{g}$, a total force of $11.8\,\mathrm{N}$ must be applied. When distributed over the four screws, this corresponds to a force of $2.95\,\mathrm{N}$ per screw. Following Eq. 2.3, we can determine the corresponding tightening torque:

$$\tau = \mu F d_{screw} = 0.6 \cdot 2.95\,\mathrm{N} \cdot 2.5\,\mathrm{mm} = 4.4\,\mathrm{N\,mm} \tag{2.7}$$

where d_{screw} is the screw diameter and μ is the friction coefficient between steel and aluminum.

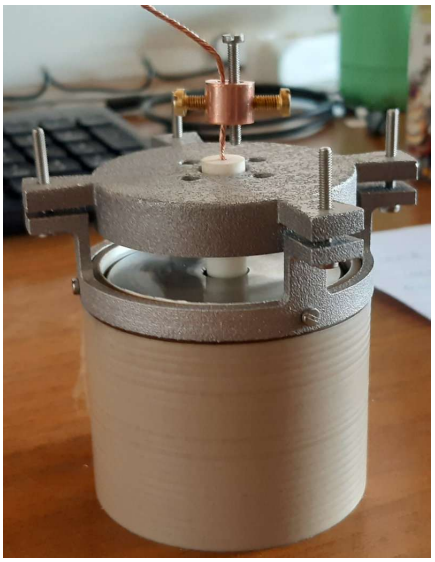

Figure 2.18: Photograph of the detector assembly (including cone, spring and spring-holder) enclosed within a cylindrical PEEK case.

The spring holder and the PEEK retaining ring are made of aluminum and were manufactured using a sintering process. This technique involves compacting metal or ceramic powders and then heating them to a temperature below their melting point. The thermal treatment promotes solid-state diffusion, causing the particles to bond and form a dense and mechanically robust component. Sintering allows the production of complex geometries that are difficult or impossible to achieve with conventional machining methods, such as milling. However, components produced by this method often retain significant surface contamination. Therefore, prior to assembly into the vacuum-compatible capsule, the sintered parts were cleaned using three ultrasonic baths in acetone to ensure proper degassing and cleanliness.

2.7 Detector Electrical Connection

Having described the mechanical infrastructure that ensures the proper operation of the HPGe detector, we now turn to the design and implementation of a reliable electrical interface for transmitting signals from the detector to the readout electronics. Due to the nanometric thickness of the PLM-doped layers, it has been critical to develop an innovative interconnection system capable of maintaining mechanical and thermal integrity, while preventing any structural or functional damage to the detector.

Several flexible printed circuit boards (PCBs) were designed and tested for this application. Referring to Fig. 2.19, we will identify them as model a, model b, and model c. Fabricated on a $36\ \mu m$ polyimide substrate, the PCBs were developed to conform closely to the geometry of the detector by wrapping around its surface, as shown in Fig. 2.20.

The PCBs have a cross-shaped design, with each arm containing three copper contact tabs[3]. These arms rest directly on the brittle, doped surface of the detector and are held

[3]The HPGe detectors developed within the framework of the N3G Project are characterized by a total of 16 electrodes: 4 are located on the top side of the detector, while the remaining 12 are distributed along the lateral side, arranged in four columns with three electrodes each. This configuration is the reason why each arm of the PCB hosts three tabs.

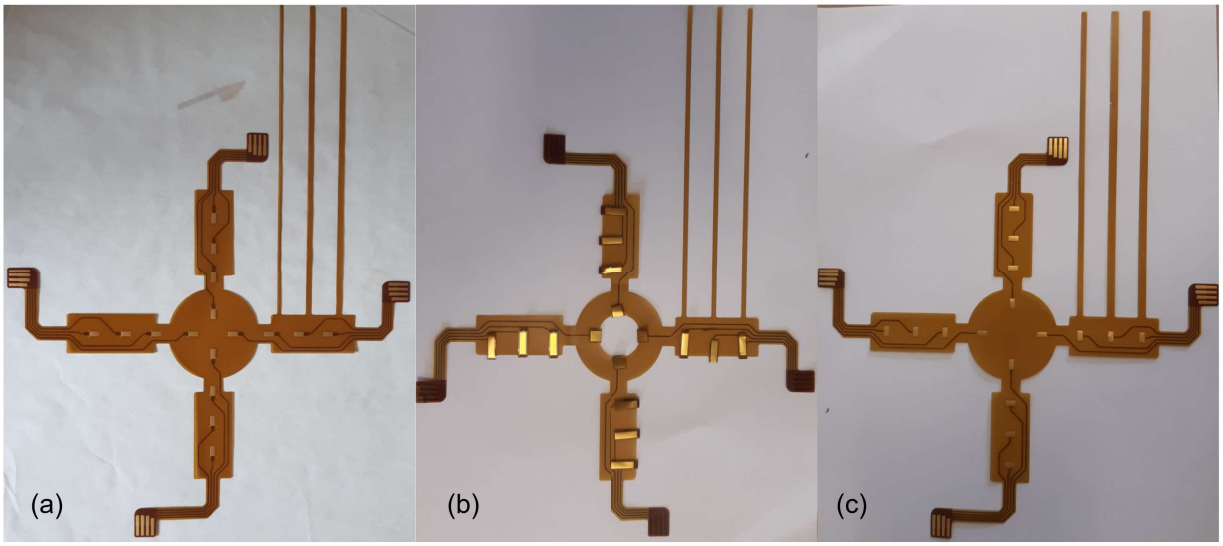

Figure 2.19: Three flexible PCB prototypes, developed to ensure a soft but reliable contact with the electrodes of a coaxial detector. Each model features a cross-shaped geometry with gold-flashed copper contact tabs on each arm. Models a and b employ folded tabs to directly press against the outer electrodes, while model c uses small indium balls placed on the tabs to establish the electrical connection.

in place by three long polyimide strips. In models a and b, the tabs housed in each arm are folded to make soft but stable contact with the electrodes, ensuring a reliable electrical connection (left and central part of Fig.2.21). In model c, by contrast, the tabs are not intended to be folded; instead, they are designed to accommodate a small indium ball that serves as point-contact with the detector electrode (right part of Fig.2.21). The electrodes on the front side of the detector are instead contacted via the tabs located in the central part of the PCBs. To improve conductivity and prevent oxidation, the copper tabs were gold-flashed. Fig. 2.22 provides a detailed view of the specific PCB components referenced in the discussion.

A digital microscope inspection of the detector's electrodes surface — conducted both before and after the application of the flexible connections — confirmed that no visible damage occurred during the procedure for model a. In contrast, the same inspection revealed that in model b the lateral folding of the contact tabs caused scratches on the electrodes surfaces, compromising their integrity. As a result, model b was found to be unsuitable and was therefore excluded from subsequent testing and application. Model c was likewise excluded, as it was not possible to remove the indium ball from the fragile electrode surface without damaging it. Model a thus emerged as the only effective and reliable prototype able to ensure a stable but soft connection without inducing mechanical damage[4].

The electrical contact performance of the proposed system (model a) was evaluated using a planar HPGe detector and compared to conventional contact methods. In particular, a commonly used configuration, consisting of a micro-spring contacting the detector surface via an interposed indium pad, was examined in detail. The analysis focused on the detector's leakage current under different reverse bias voltages, as shown

[4]This soft connection could also be used with HPGe detectors made with standard doping techniques. In this framework, key advantages may lie in the ease of integrating and removing the contact system, along with its robustness under the thermal cycling conditions these detectors undergo together with the annealing operations.

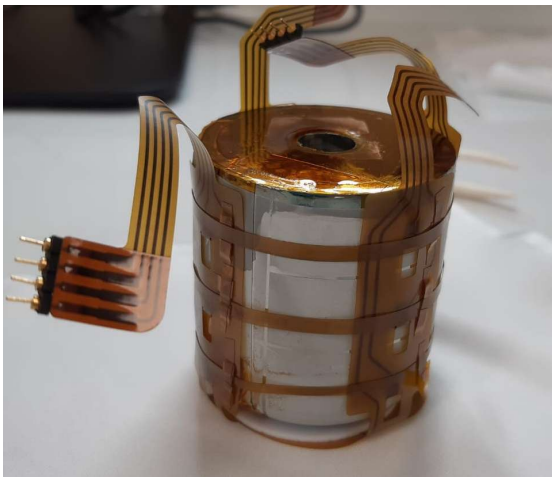

Figure 2.20: Flexible PCB connecting the electrodes of the detector. Each arm of the PCB lies on the doped surface and is held in place by three long polyimide strips wrapped around the detector itself.

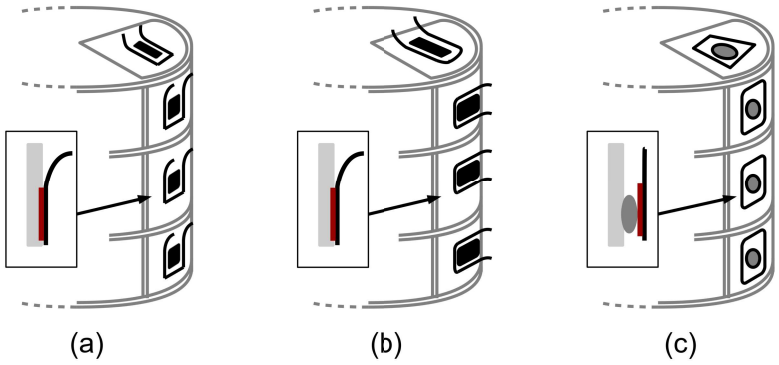

Figure 2.21: Schematic of the different contact types in PCB models a, b, and c. In models a and b, the tabs are folded to press against the detector electrodes. In model c, the tabs remain unfolded and hold a small indium ball, which serves as a point-contact with the detector electrodes.

in Fig. 2.23. The results demonstrate that the proposed solution significantly reduces leakage current at high bias voltages, which are required to fully deplete the active volume of the HPGe detector[5].

Signals from the flexible PCB wrapped around the detector are then routed to the flange feed-through connectors via a rigid PCB with ceramic substrate, as shown in Fig. 2.24. This rigid PCB was soldered directly onto the electrical feed-through connectors on the flange. Each feed-through is connected to a row of seven pin headers, where pins from the flexible PCB can be quickly plugged. This connection method was designed for speed and simplicity, essential for minimizing the time the germanium detector is exposed to the atmosphere during assembly.

On the outer side of the capsule, two rigid crescent-shaped PCBs enable the distribution of signals to the read-out electronics, as shown in Fig. 2.25. The first PCB connects

[5]It is worth noting that the conventional contacting approach, which employs a micro-spring in contact with the detector surface through an interposed indium pad, does not produce leakage currents as high as those observed in our setup. This can be attributed to the substantially thicker doped regions in detectors fabricated with standard processing techniques, where microscopic damage is not induced to the contact interface.

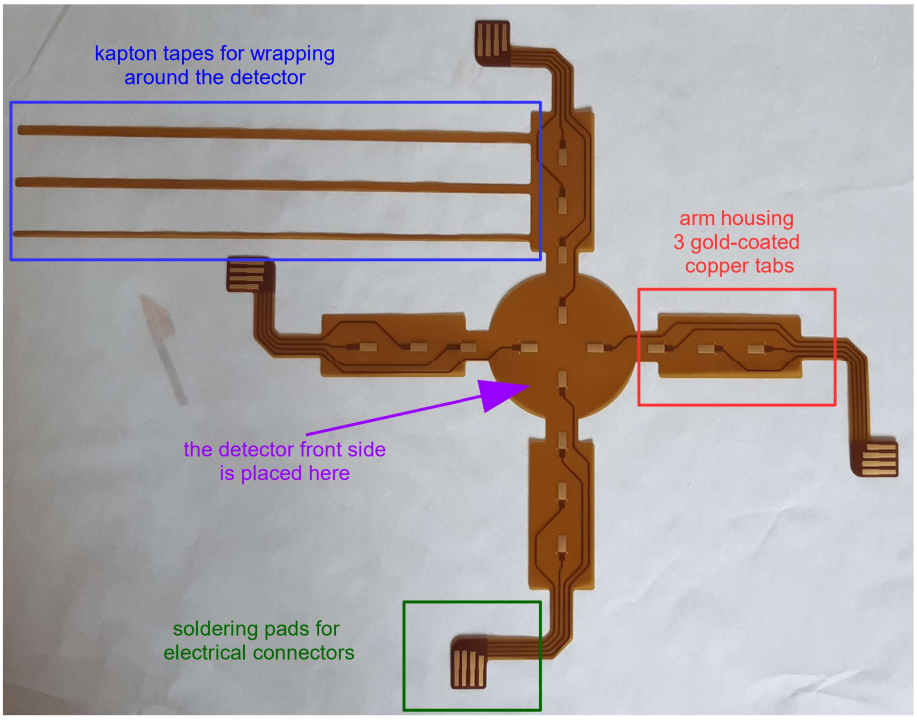

Figure 2.22: Flexible PCB featuring a detailed overview of the electrical connection elements it integrates.

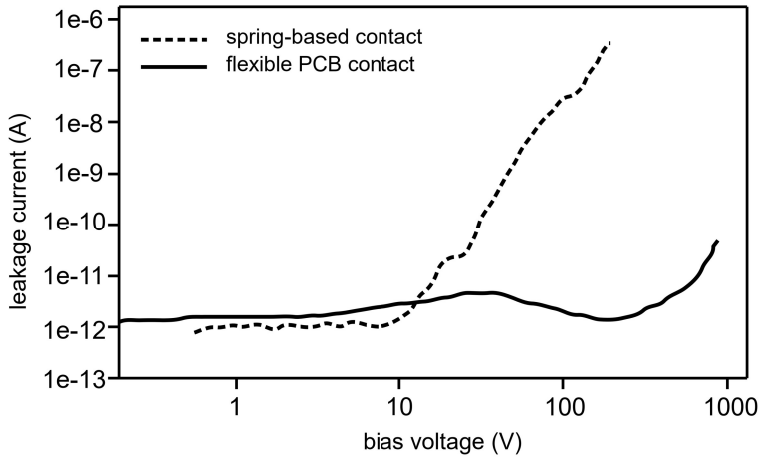

Figure 2.23: Comparison of leakage current measurements using a traditional contact system with a micro-spring (dashed line) versus the flexible PCB-based system developed (solid line). This test was carried out on an HPGe detector which under typical conditions operates with a reverse bias voltage of approximately 1 kV.

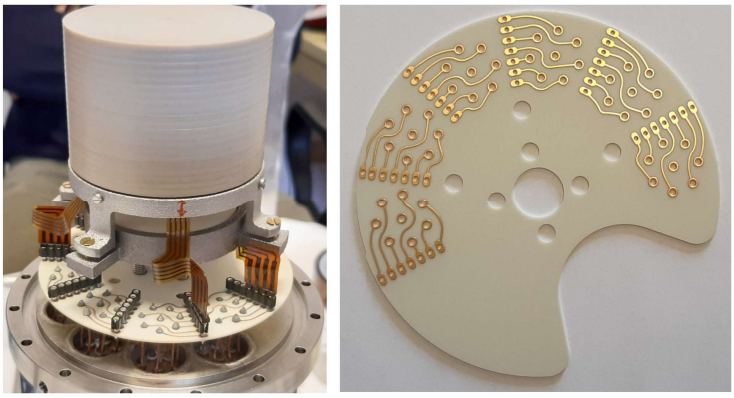

Figure 2.24: Ceramic PCB routing the flexible PCB to the flange feed-through connectors. The number of connections is intentionally over-sized to allow for future application with detectors featuring a larger number of electrodes.

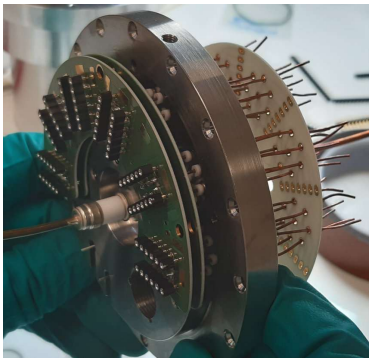

Figure 2.25: Photograph of the flange with the rigid PCBs required to interface the electrical feed-through connectors with the block-FETs, which host the input transistor of the charge-sensitive preamplifier and the feedback network.

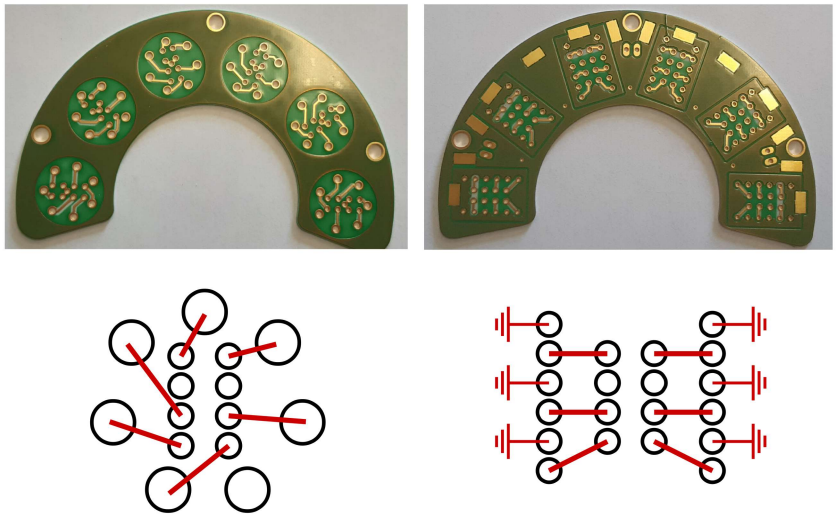

Figure 2.26: Photographs and connection diagram of the rigid PCBs mounted on the outer side of the capsule. Their shape is specifically designed to allow the capsule to be mounted onto the cold finger.

six out of the seven[6] leads of each feed-through to an 8-pin connector. A second PCB, designed to be plugged onto the first one, routes these six signals to a 12-pin connector in which signal lines are alternated with ground lines, as illustrated in Fig. 2.26. This connector follows the standard interface used in AGATA detector capsules [10] and is designed to accommodate a block-FET module. The block-FET consists of a compact Faraday cage housing the input transistor, the feedback resistor and the feedback capacitor of six state-of-the-art CSPs, one for each signal coming from a feed-through connector. The block-FET is thermally coupled to the capsule to cool down its electronic components and significantly reduce their thermal noise. From the block-FET, signals are finally routed to the cryostat flange and distributed to the preamplifiers housed outside the cryostat end cap.

2.8 Detector Assembly Procedure

Having detailed both the mechanical set-up and the electronic read-out connections, we can now describe the complete assembly procedure we developed for the coaxial and segmented HPGe detector.

After the passivation process, the detector is placed at the center of the flexible PCB[7], with its upper electrodes facing the board. Then, the four arms of the PCB are brought into contact with the lateral surface of the detector and secured by means of the three polyimide strips previously introduced. These strips must be carefully wrapped around the detector and fastened with polyimide tape, (Fig. 2.27a). Afterward, the detector is inserted in the PEEK case and the holder is removed (Fig. 2.27b). At this stage, the alumina cone housing the high-voltage connector can be inserted into the cavity (Fig. 2.27c) and the single-wave spring can be positioned at the cone base (Fig. 2.27d). The assembly is completed by positioning the spring holder and fastening it to the PEEK case using a torque screwdriver to apply the calculated tightening torque (Fig. 2.27e and 2.27f). As can be seen, the spring holder must already be screwed onto the flange in the correct position to enable a quick and efficient assembly procedure. This step is completed by securing the high-voltage contact to the rod on the flange using the dedicated clamp. At the end of this assembly sequence, the detector is securely positioned and can be moved and rotated without risk. This allows the flange to be mounted onto the cryostat's cold finger and sealed with the corresponding canister, as illustrated in Fig. 2.28.

2.8.1 First Tests Performed with a Detector

The system we designed allowed for the testing of detectors developed in the framework of the N3G project. In what follows, we will specifically focus on the results obtained from a commercial crystal that was reprocessed using the PLM technique.

The detector consists of a n-type HPGe crystal with an external diameter of $51.3\,\mathrm{mm}$ and a height of $44.5\,\mathrm{mm}$. It features an inner lithium-diffused core approximately $36.5\,\mathrm{mm}$ deep and about $9\,\mathrm{mm}$ wide. The detector's bottom surface, being passivated, was carefully protected with a polyimide sheet during the crystal reprocessing to preserve its integrity.

[6] Each feed-through connector originally features eight leads; however, the central pin was physically removed to reduce mechanical interference and accommodate the limited available space.

[7] The detector is moved using a dedicated sample holder, designed to support the crystal from its inner cavity. The holder consists of a hollow PTFE tube with a conical termination, containing a central threaded metal shaft that extends from both ends. A series of expandable O-rings are positioned along the shaft to grip and firmly hold the crystal inside its cavity, ensuring stable support during manipulation.

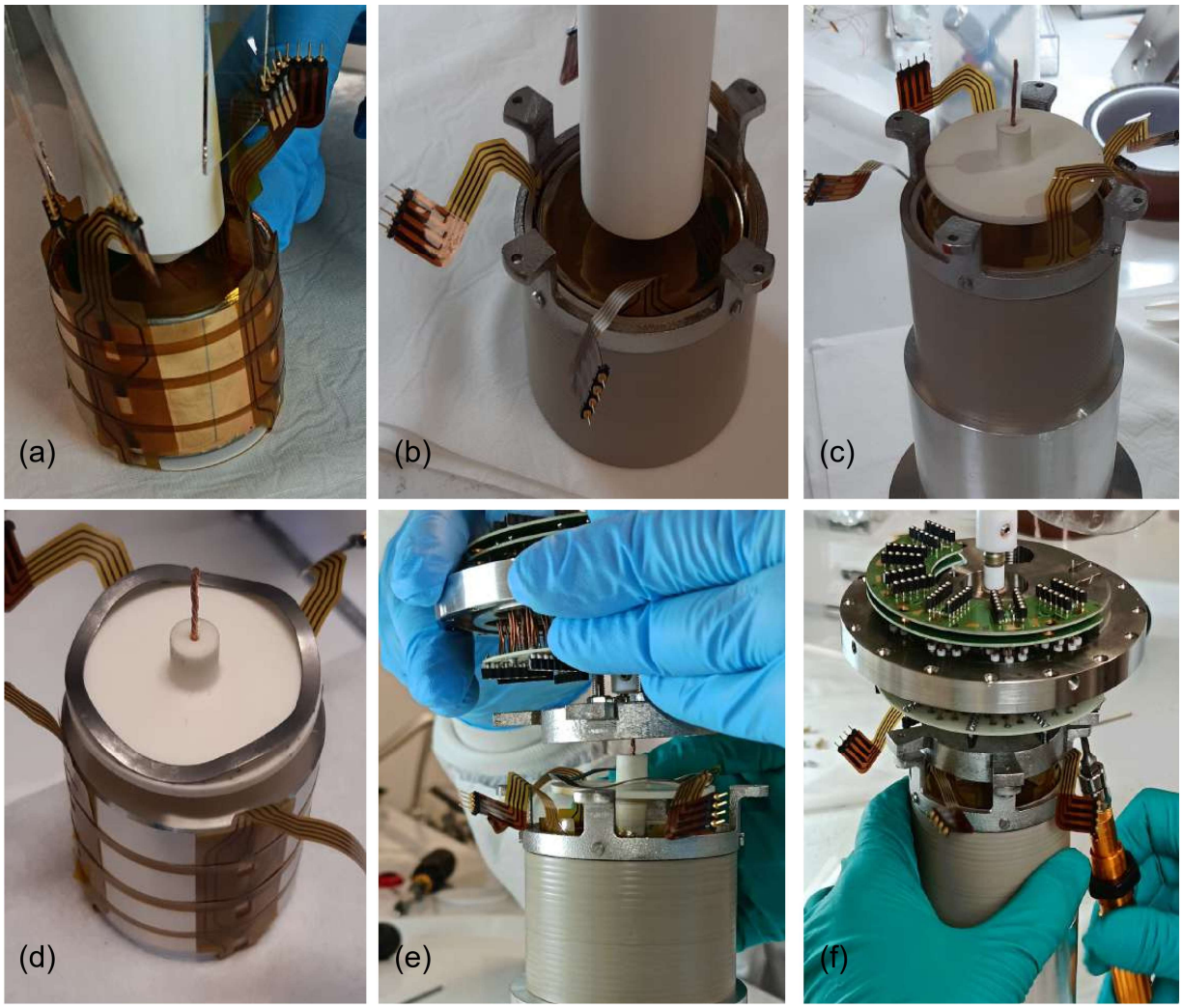

Figure 2.27: Step-by-step illustration of the detector assembly process. (a) The four arms of the flexible PCB are brought into contact with the lateral surface of the detector and secured using the three polyimide strips. The strips are carefully wrapped around the detector and fastened with polyimide tape. (b) The detector is then inserted into the PEEK case and the temporary holder is removed. (c) The alumina cone housing the high-voltage connector is inserted into the cavity. (d) The single-wave spring is positioned at the base of the cone. (e–f) The assembly is completed by positioning the spring holder and fastening it to the PEEK case using a torque screwdriver set to the calculated tightening torque.

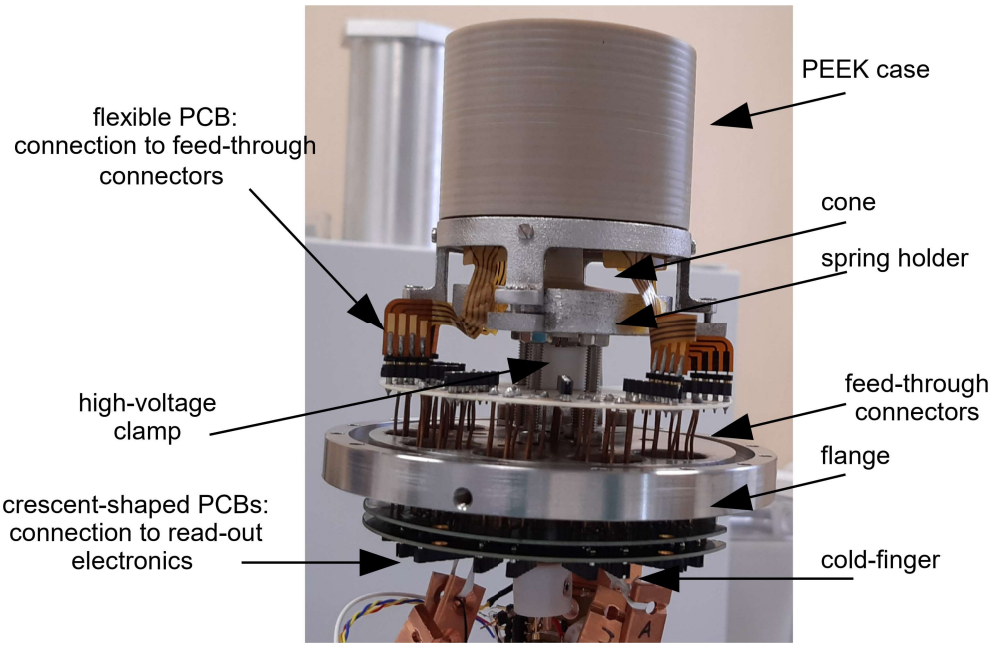

Figure 2.28: Photograph of a detector mounted on the cold finger of the CTT cryostat (Cryostat Technology Thomas, Germany) at the Legnaro National Laboratories.

First of all, the external surface of the detector underwent polishing, followed by quenching in bi-distilled water and drying with nitrogen to ensure a clean and smooth finish. For the doping process, aluminum-germanium precursors were used as p-type dopants and deposited. After deposition, the sample was transferred to the PLM facility, where the aluminum PLM junction was realized. Thereafter, a gold layer of approximately $100\,\mathrm{nm}$ - $300\,\mathrm{nm}$ was deposited on the crystal lateral and top surface. The sample was then mounted on a rotor capable of rotating it along its longitudinal axis to allow uniform spray-coating of photo-resist over its entire external surface. After a baking step to harden the resist, the sample was transferred to another rotor where a six-joint robotic arm equipped with a UV laser was employed to expose the positive photo-resist. By synchronizing the laser movement with the sample rotation, the desired segmentation pattern was defined on the crystal surface, as shown in Fig. 2.29. As can be seen, the crystal was divided into twelve segments: the four upper lateral ones were not separated from the four on the top surface.

After UV exposure, the sample was developed and the gold between segments was selectively removed with the dedicated gold etchant. The remaining photo-resist was then stripped with acetone and chemical passivation of the trenches was carried out with methanol. Unfortunately, at this stage of the process, the gold etchant removed part of the gold layer on the top surface, directly exposing the junction and unifying the top segments together. Nevertheless, the detector was properly mounted according to the procedure previously described, but, on the top surface, direct contact between the flexible PCB copper tabs and the junction was avoided by inserting a Teflon disk between them. The entire process was performed in an ISO-7 clean room environment, while maintaining a continuous argon flow over the crystal.

After completing the assembly operations, the capsule was mounted onto the cold finger of the cryostat. At this stage, we verified that all the tabs on the arms of the flexible PCB were in proper contact with the detector. This was done by measuring the resistance between the core and the segments. At room temperature, germanium

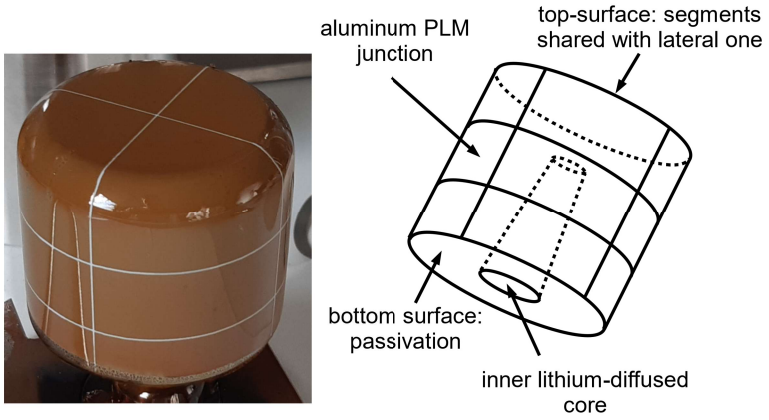

Figure 2.29: On the left, n-type commercial crystal, reprocessed using the PLM technique, after the photolithography stage. On the right, schematic representation of its segmentation and parts.

behaves essentially as a conductor; therefore, contact integrity can be assessed via resistance measurements. Values on the order of tens of ohms were observed, confirming good electrical contact between the PCB and the detector electrodes.

Due to an issue with the surface finish of the capsule flange, vacuum could not be applied directly to the capsule. As a result, a second capsule was later fabricated with improved flange finishing. In the meantime, the vacuum of the cryostat itself was used to properly operate the detector. To achieve a vacuum level on the order of $10^{-6}\,\mathrm{mbar}$, the cryostat was pumped for approximately two days[8].

At the end of this period, the crystal was cooled down at liquid nitrogen temperature (77 K) and tested. Two main types of measurements were carried out. The first was the current–voltage (I–V) characterization. In this measurement, the voltage applied to the cavity was varied, and the leakage current from each segment was individually measured using a precision ammeter and grounding all the other segments. The second measurement, on the other hand, focused on determining the resistance between adjacent segments. A constant $10\,\mathrm{V}$ voltage was applied to the cavity, and the reference segment was grounded. All other segments were grounded as well, except for the one directly adjacent to the reference segment — the target segment for the resistance measurement. A small bias voltage, on the order of $100\,\mathrm{mV}$, was applied to this target segment to induce a current between the two. By measuring the resulting current and knowing the voltage difference, the resistance between the adjacent segments was calculated.

From the current–voltage measurements, we obtained the results reported in Fig. 2.30.

- The top segments of the crystal, shorted together, exhibited a high leakage current (greater than $1\,\mu\mathrm{A}$), primarily due to the issue identified during the etching process.
- The bottom segments exhibited high leakage currents too, ranging from $50\,\mu\mathrm{A}$ to

[8]Cryostats are typically pumped over this period to achieve high vacuum levels, as degassing from internal surfaces and components is a common issue. To minimize degassing, exposure to atmospheric pressure should be kept as brief as possible and only occur under clean room conditions. Furthermore, the cryostat should be periodically baked to desorb residual gases. Annealing temperatures must remain below 130,°C to prevent damage to feed-through connectors.

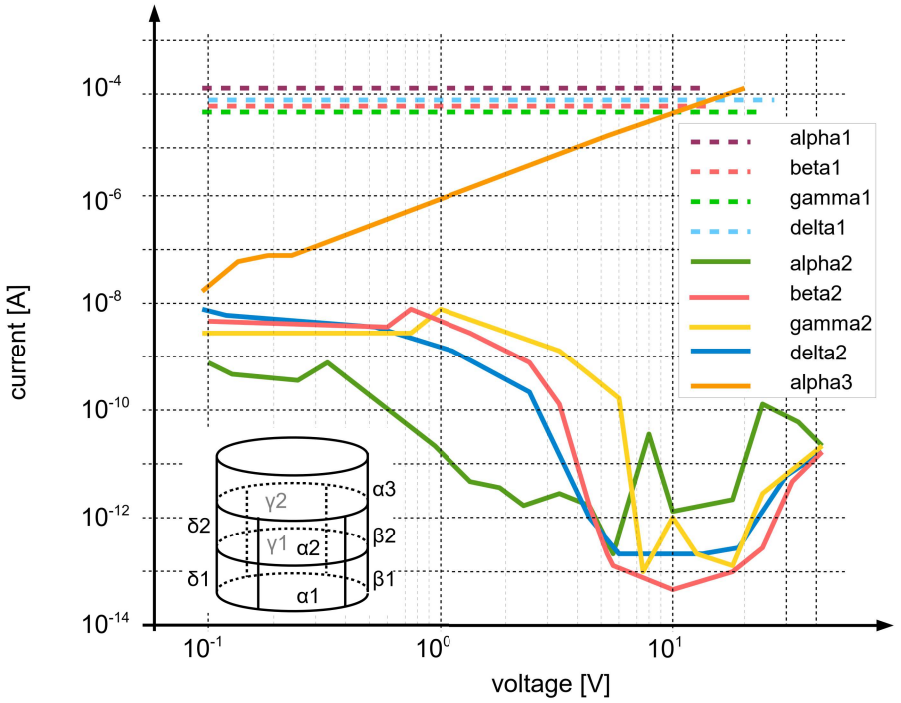

Figure 2.30: Segment-by-segment trend of the leakage current for different bias voltage values applied to the detector cavity.

$90\,\mu A$ even without biasing the detector. We believe that they are most likely due to an issue that occurred during the gold deposition process, when some gold was inadvertently deposited onto the passivated surface of the crystal. As a consequence, these compromised segments behave like short-circuited diodes, leading to the observed high leakage currents.

- The middle segments exhibited the most promising behavior. When a bias voltage of a few tens of millivolts was applied to the cavity, the measured leakage current was approximately $10\,nA$. As the bias increased to $1\,V$, the current dropped significantly, reaching values in the picoampere range. This low current remained stable as the voltage increased further, up to about $40\,V$–$45\,V$[9]. The observed current profile suggests that, at low bias, the surface region of the diode is only partially depleted, resulting in higher leakage currents. As the voltage increases and the surface becomes fully depleted, the leakage current drops sharply, indicating improved junction performance in the middle segments.

Resistance measurements between segments were carried out on the middle region of the crystal, where the leakage current was sufficiently low to allow reliable readings. We measured values on the order of $10\,T\Omega$ between adjacent lateral segments, and a few $T\Omega$ between middle and top or middle and bottom segments. These high resistance values are consistent with expectations and provide strong evidence that the trenching process successfully ensured electrical isolation between segments.

[9]Beyond this threshold, however, measurements had to be interrupted due to a sharp increase in leakage current from the top segments, which caused the overall power consumption to rise, posing a potential risk to the instrumentation.

Unfortunately, the limited bias voltage applicable to the detector, due to the $40\,\mathrm{V}$–$45\,\mathrm{V}$ breakdown, prevented us from performing charge collection measurements with a radioactive source and acquiring meaningful spectra. Although the crystal was subjected to a second reprocessing, subsequent chemical treatments after photolithography repeatedly damaged its surface finish, hindering any further significant measurements. Despite these setbacks, the work will continue with a focus on optimizing the detector processing steps to improve surface integrity and overall performance.

However, the flexible connection system we developed for the detector demonstrated reliable functionality throughout the experiments, and the custom mechanical support structure proved robust and well-suited to the setup. These successful elements provide a solid foundation for future efforts and encourage confidence that, with refined fabrication protocols, the detector will achieve its intended performance. The lessons learned here will guide ongoing improvements, ultimately contributing to the advancement of high-precision detector technologies.

CHAPTER 3

Front-End Electronics for Solid-State Detectors

The Charge Sensitive Preamplifier (CSP) is the first circuit block of a typical signal acquisition chain for radiation detectors. It integrates the current induced on the detector electrode to which it is connected and converts it into an analog voltage signal that can be processed in different ways.

In classical analog systems, signals are processed by spectroscopy shaping amplifiers, which are designed to convert the CSP output signals into Gaussian-shaped pulses (Fig. 3.1). These amplifiers typically include a baseline restorer, making them insensitive to fluctuations in the signal baseline. Their main purpose is to optimize the signal-to-noise ratio (SNR) and they offer adjustable shaping times, typically ranging from $0.1\,\mu s$ to $10\,\mu s$.

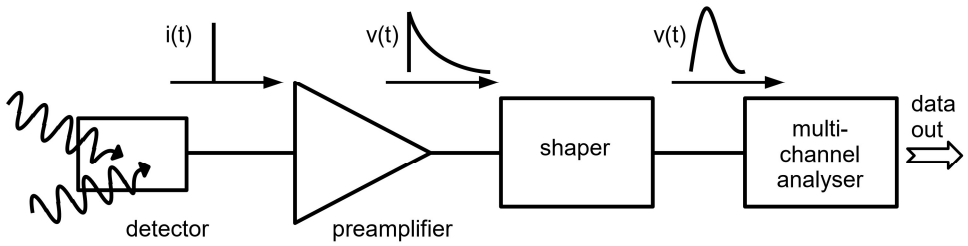

Figure 3.1: Classical spectroscopic read-out chain.

On the other hand, modern approaches involve digitally sampling the preamplifier output waveform [29]. In this case, the decay time constant of the preamplifier is usually removed using moving-window deconvolution algorithms. The processed signals are then shaped using trapezoidal filters to extract energy information. For applications such as particle identification or gamma-ray tracking with high-purity germanium (HPGe) detectors, direct analog-to-digital conversion of the preamplifier output is often employed, followed by dedicated offline digital processing algorithms.

In some setups, the preamplifier signals are processed in real-time using analog or digital algorithms, and only key parameters such as energy and rise-time are stored. In others, the full waveform of each event is recorded, requiring more sophisticated front-end and back-end architectures. Despite the increased complexity, this approach offers maximum flexibility, allowing researchers to apply customized analysis algorithms offline, without being limited by decisions made during data acquisition.

3.1 Shockley-Ramo's Theorem and Signals Formation

A clear understanding of signal formation in solid-state detectors is crucial for optimizing the design and performance of the read-out electronic chain.

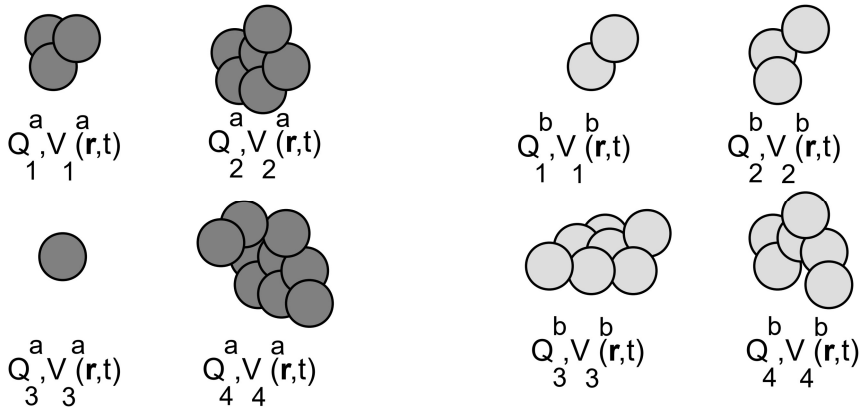

Figure 3.2: Independent distributions of discrete charge and associated potentials.

Signal generation extends beyond the simplistic view of mere charge collection. Rather, it arises from the variation over time of the electrostatic flux through the electrode surface due to the charge carriers motion within the detector volume. This principle is formalized by Shockley-Ramo's theorem [30][31], which states that the induced current on an electrode depends only on the position and velocity of the moving charges, the detector geometry and the boundary conditions, and is quantified through the so-called weighting field. This implies that a moving charge induces signals on electrodes as long as it drifts inside the detector itself until it is physically collected at an electrode or trapped.

Shockley-Ramo's theorem is based on Green's reciprocity theorem [32]. Let us take, for instance, two different and independent charge distributions, $\rho_1(\mathbf{r})$ and $\rho_2(\mathbf{r})$, and the potential they respectively generate, $V_1(\mathbf{r},t)$ and $V_2(\mathbf{r},t)$. We consider them separately, one at a time t. It follows that (Appendix A):

$$\int \rho_1(\mathbf{r})V_2(\mathbf{r},t)d^3\mathbf{r} = \int \rho_2(\mathbf{r})V_1(\mathbf{r},t)d^3\mathbf{r} \tag{3.1}$$

This result can also be extended to a discrete system of charges, like the one depicted in Fig.3.2. In this case, any charge density $\rho(\mathbf{r})$ can be expressed as:

$$\rho(\mathbf{r}) = \sum_i Q_i \delta(\mathbf{r} - \mathbf{r}_i) \tag{3.2}$$

where Q_i is the charge located at the position $\mathbf{r}_i$. Thus, we can write:

$$\sum_i Q_i^a V^b(\mathbf{r}_i,t) = \sum_j Q_j^b V^a(\mathbf{r}_j,t) \tag{3.3}$$

Let us consider a system consisting of k grounded electrodes, each carrying a charge Q_i, as illustrated in Fig. 3.3a. A point P lies between these electrodes, and a charge q_p is placed at this point. The electric potential at point P in this configuration is denoted by V_p^a. Now, suppose the charge q_p at point P is removed, and instead an electric potential V_k^b is applied to the k-th electrode, as shown in Fig. 3.3b. By applying the discrete form of Green's theorem (Eq. 3.3), it follows that:

$$\begin{bmatrix} q_p \\ Q_1^a \\ Q_2^a \\ .. \\ Q_k^a \end{bmatrix} \cdot \begin{bmatrix} V_p^b \\ 0 \\ 0 \\ .. \\ V_k^b \end{bmatrix} = \begin{bmatrix} 0 \\ Q_1^b \\ Q_2^b \\ .. \\ Q_k^b \end{bmatrix} \cdot \begin{bmatrix} V_p^a \\ 0 \\ 0 \\ .. \\ 0 \end{bmatrix} \Rightarrow q_p V_p^b + Q_k^a V_k^b = 0 \tag{3.4}$$

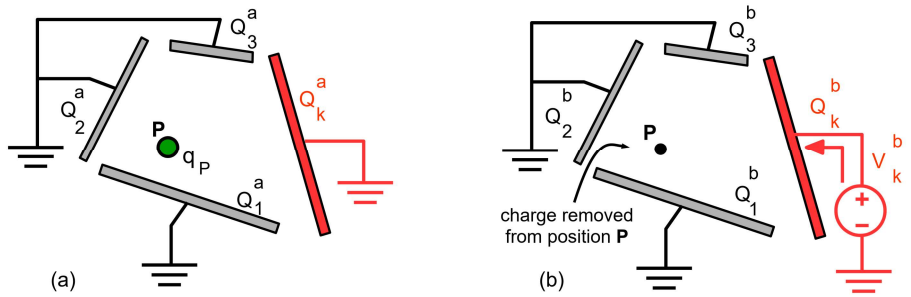

Figure 3.3: (a) System consisting of k grounded electrodes carrying charges Q_i. A charge q_p is placed at point P. (b) In the same system, the charge q_p is removed and an electric potential is applied to the k-th electrode.

By defining the weighting potential $\tilde{V}_w$ as the following ratio,

$$\tilde{V}_w = \frac{V_p^b}{V_k^b}\,, \tag{3.5}$$

we can write the expression for the induced charge on the k^{th} electrode by the charge q_p:

$$Q_k^a = -q_p \tilde{V}_w \tag{3.6}$$

By differentiating both sides of this equation with respect to time, we obtain the expression for the induced current[1] on the electrode taken into account:

$$i_k = -q_p \frac{d}{dt}\tilde{V}_w = -q_p \frac{d}{dt}\tilde{V}_w \frac{dl}{dl} = q_p \mathbf{E}_w \mathbf{v} \tag{3.7}$$

As reported in Eq. 3.7, the induced current depends on the charge released inside the detector, its velocity and the weighting field $\mathbf{E}_w$. The weighting field can be practically evaluated using the same relations that allow the calculation of the electric field, but by setting the potentials of all electrodes to zero except for the k^{th} one, which is set at 1[2].

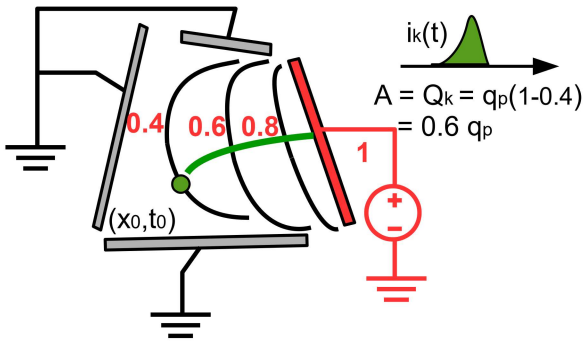

Figure 3.4: Weighting potential map and induced charge calculation.

It is important to emphasize that, starting from the weighting potential map, the induced charge can be easily calculated as follows:

$$Q_k(t) = \int_0^t i_k(\tau)d\tau = \int_0^t q_p \frac{d\mathbf{x}}{d\tau}\mathbf{E}_w d\tau = q_p \int_{x_0}^{x} \mathbf{E}_w d\mathbf{x} \tag{3.8}$$

[1]Here, the relationship is expressed with a positive sign because the current is outgoing. In the case of incoming current, the same relationship must be written with a negative sign.

[2]The potential is set to 1, not 1 V: the weighting field is dimensionally the inverse of a length.

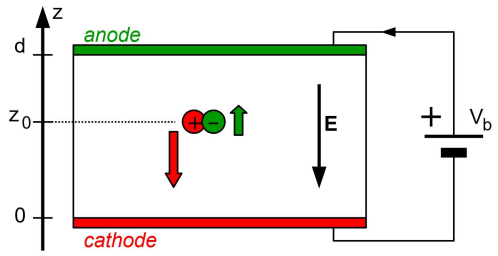

Figure 3.5: Point-like charge within a planar detector geometry.

As a consequence,

$$Q_k(t) = -q_p[\tilde{V}_w(x) - \tilde{V}_w(x_0)]. \tag{3.9}$$

Therefore, signals evaluation at a given electrode involves the following steps [33]:

- determining the initial spatial distributions of electrons and holes generated by the photon or charge particle interaction;
- analyzing the motion of these charge carriers in the electric field, which is shaped by both the applied bias voltage and the space charge from doping atoms. The space charge from ionization-generated carriers can be neglected for minimum-ionizing particles;
- calculating the contribution of each moving charge element to the signal, using a weighting field. This field depends on the detector's geometry, the connected electronic circuitry, and the velocity of the charge element being considered.

3.1.1 Current and Charge Induced in a Planar Detector Geometry

Let us consider a reverse-biased planar detector, as depicted in Fig. 3.6. Under the approximation of parallel-plate capacitor, the electric field inside the detector is:

$$\mathbf{E} = -\frac{V_b}{d}\hat{\mathbf{u}}_z \tag{3.10}$$

Now, let us suppose that a photon interacts within the detector. Unlike charged particles, which ionize continuously along their path, it undergoes a point-like interaction, locally releasing electron-hole pairs with a total charge Q proportional to its energy. Because of the applied electric field, electrons move to the anode, while holes to the cathode, with velocities

$$\mathbf{v}_e = -\mu_e \cdot (-\frac{V_b}{d}\hat{\mathbf{u}}_z) = \mu_e \cdot \frac{V_b}{d}\hat{\mathbf{u}}_z \tag{3.11}$$

$$\mathbf{v}_h = -\mu_h \cdot \frac{V_b}{d}\hat{\mathbf{u}}_z \tag{3.12}$$

respectively. Here μ_e and μ_h are the mobilities of electrons and holes. For instance, in room-temperature germanium [34],

$$\mu_e = 3900\,\mathrm{cm}^2\,\mathrm{V}^{-1}\,\mathrm{s}^{-1} \tag{3.13}$$

$$\mu_h = 1900\,\mathrm{cm}^2\,\mathrm{V}^{-1}\,\mathrm{s}^{-1} \tag{3.14}$$

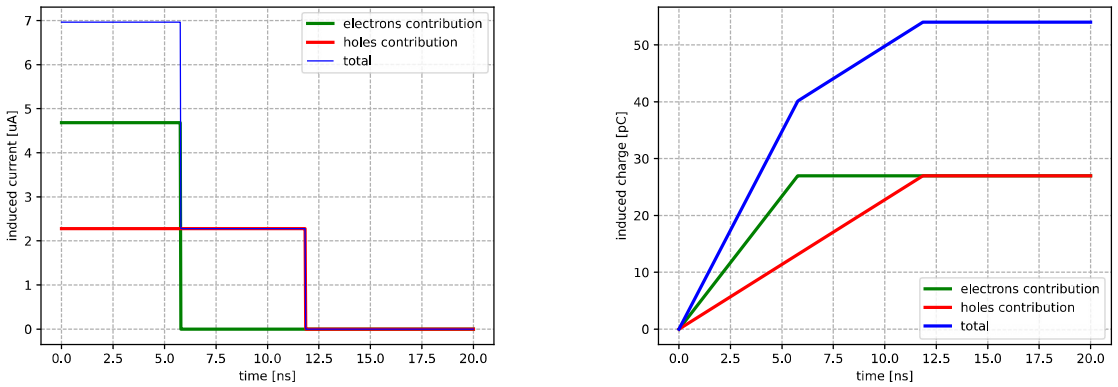

(a) Current induced by the point-like charge

(b) Charge induced by the point-like charge

Figure 3.6: Simulation of the induced current and charge generated by a $1\,\mathrm{MeV}$ photon interacting at the midpoint of a planar germanium detector $3\,\mathrm{mm}$ thick and reverse-biased with a $2\,\mathrm{kV}$ potential.

To find the current induced on the anode by both types of charge carriers, we start evaluating the weighting field. We set the anode potential to 1 and that of cathode to 0:

$$\mathbf{E}_w = -\frac{1}{d}\hat{\mathbf{u}}_\mathbf{z} \tag{3.15}$$

By applying Ramo's theorem (Eq.3.7), we obtain:

$$i_e = -Q\mu_e \frac{V_b}{d} \cdot (-\frac{1}{d}) = Q\mu_e \frac{V_b}{d^2} \tag{3.16}$$

$$i_h = Q(-\mu_h \frac{V_b}{d}) \cdot (-\frac{1}{d}) = Q\mu_h \frac{V_b}{d^2} \tag{3.17}$$

Since the velocities are constant, the times of flight of electrons and holes can be written as:

$$t_e = \frac{d - z_0}{v_e} = d\frac{d - z_0}{\mu_e V_b} \tag{3.18}$$

$$t_h = \frac{z_0}{v_h} = d\frac{z_0}{\mu_h V_b} \tag{3.19}$$

By using these values as the integration limits of the total current, defined as the sum of electron and hole contributions, the total charge induced on the anode is finally determined:

$$Q(t) = \int (i_e + i_h)dt = \begin{cases} Q(\mu_e + \mu_h)\dfrac{V_b}{d^2} \cdot t & \text{if } t < t_e \\ Q(\mu_e + \mu_h)\dfrac{V_b}{d^2} t_e + Q\mu_h \dfrac{V_b}{d^2} \cdot t & \text{if } t_e < t < t_h \end{cases} \tag{3.20}$$

As an example, Fig. 3.6 shows the induced current - 3.6(a) - and charge - 3.6(b) - resulting from the interaction of a $1\,\mathrm{MeV}$ photon in a planar germanium detector, $3\,\mathrm{mm}$

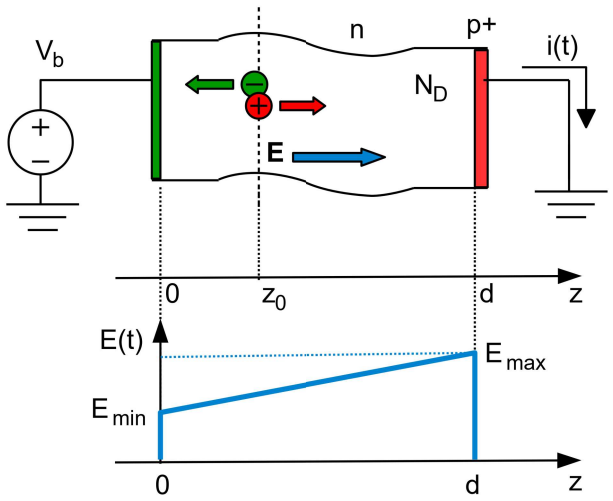

Figure 3.7: Point-like charge within a pn-junction.

thick, assuming the interaction occurs at the midpoint of the detector. As can be seen, the current pulses have a temporal width of a few nanoseconds, which is significantly shorter than typical spectroscopic timescales (several microseconds) of signal processing electronics. This allows us to approximate these pulses as delta-like functions.

It is also noteworthy that interactions occurring in proximity to the anode produce only a negligible electron-induced charge. Consequently, the total induced charge is largely due to holes, which must drift through the full detector volume, leading to a significantly longer rise time in the induced signal. Furthermore, holes have a higher probability of being trapped [35] potentially leading to a significant charge deficit.

3.1.2 Current and Charge Induced in a pn-Junction

Let us take into account an over-depleted reverse-biased pn-junction, as reported in Fig. 3.7. Moreover, let's assume that the p-type region is much more heavily doped than the n-type one and that the donor atoms concentration is N_D. As before, we consider the interaction of a photon resulting in the creation of a point charge Q. The electric field can be evaluated by applying the Gauss law:

$$\nabla \mathbf{E} = \frac{\rho}{\epsilon} = q\frac{N_D}{\epsilon} \tag{3.21}$$

$$\frac{\partial E_x}{\partial x} + \frac{\partial E_y}{\partial y} + \frac{\partial E_z}{\partial z} = q\frac{N_D}{\epsilon} \Rightarrow E_z(z) = \int_0^z q\frac{N_D}{\epsilon} d\xi = q\frac{N_D}{\epsilon} z + E_{min} \tag{3.22}$$

with q the elementary charge and ϵ the medium dielectric constant. Because of the non-uniform electric field, holes move toward the cathode with velocity $\mathbf{v}_h$ which depends on the z position:

$$\mathbf{v}_h = \mu_h \mathbf{E}_z = \left(\mu_h \frac{qN_D}{\epsilon} z + \mu_h E_{min}\right)\hat{\mathbf{u}}_z \tag{3.23}$$

This is a first-order differential equation whose solution is:

$$z(t) = -\frac{\epsilon}{qN_D} E_{min} + (z_0 + \frac{\epsilon}{qN_D} E_{min}) \cdot \exp\left(\mu_h \frac{qN_D}{\epsilon} t\right) \tag{3.24}$$

with z_0 the interaction point. By substituting Eq. 3.24 in Eq. 3.23, we obtain:

$$\mathbf{v}_h(t) = \mu_h(E_{min} + \frac{qN_D}{\epsilon}z_0) \cdot \exp\left(\mu_h \frac{qN_D}{\epsilon}t\right)\hat{\mathbf{u}}_\mathbf{z} \tag{3.25}$$

In order to evaluate the current and the charge induced on the cathode, we can write the weighting field as:

$$\mathbf{E}_w = -\frac{1}{d}\hat{\mathbf{u}}_\mathbf{z} \tag{3.26}$$

Hence, the hole contribution to the induced current is:

$$i_h(t) = \frac{\mu_h Q}{d}(E_{min} + \frac{qN_D}{\epsilon}z_0) \cdot \exp\left(\mu_h \frac{qN_D}{\epsilon}t\right) \tag{3.27}$$

By integrating this last equation over time, the hole contribution $Q_h(t)$to the induced charge at time t is obtained:

$$Q_h(t) = \int_0^t i_h(\tau)d\tau = \frac{Q\epsilon}{qN_D d}\left(E_{min} + \frac{qN_D}{\epsilon}z_0\right)\left[\exp\left(\mu_h \frac{qN_D}{\epsilon}t\right) - 1\right] \tag{3.28}$$

The hole total contribution is finally determined replacing t with the time of flight t_h. To evaluate t_h, we can use Eq. 3.24 and the condition $z(t_h) = d$, which leads to:

$$t_h = \frac{\epsilon}{q\mu_h N_D} \cdot ln\left(\frac{d + \epsilon E_{min}/qN_D}{z_0 + \epsilon E_{min}/qN_D}\right) \tag{3.29}$$

Substituting this result in Eq. 3.28, we find:

$$Q_h = \frac{Q}{d}(d - z_0) \tag{3.30}$$

By repeating the same steps, the electrons contribution to the induced current and charge can be determined.

$$z(t) = -\frac{\epsilon}{qN_D}E_{min} + (z_0 + \frac{\epsilon}{qN_D}E_{min}) \cdot \exp\left(-\mu_h \frac{qN_D}{\epsilon}t\right) \tag{3.31}$$

$$\mathbf{v}_e(t) = -\mu_e(E_{min} + \frac{qN_D}{\epsilon}z_0) \cdot \exp\left(-\mu_e \frac{qN_D}{\epsilon}t\right)\hat{\mathbf{u}}_\mathbf{z} \tag{3.32}$$

$$i_e(t) = \frac{\mu_e Q}{d}(E_{min} + \frac{qN_D}{\epsilon}z_0) \cdot \exp\left(-\mu_e \frac{qN_D}{\epsilon}t\right) \tag{3.33}$$

$$Q_e(t) = \int_0^t i_e(\tau)d\tau = -\frac{Q\epsilon}{qN_D d}\left(E_{min} + \frac{qN_D}{\epsilon}z_0\right)\left[\exp\left(-\mu_e \frac{qN_D}{\epsilon}t\right) - 1\right] \tag{3.34}$$

$$t_e = -\frac{\epsilon}{q\mu_e N_D} \cdot ln\left(\frac{\epsilon E_{min}/qN_D}{z_0 + \epsilon E_{min}/qN_D}\right) \tag{3.35}$$

$$Q_e = Q\frac{z_0}{d} \tag{3.36}$$

Simulation of the induced current and charge resulting from the interaction of a $1\,\mathrm{MeV}$ photon at the midpoint of a $10\,\mathrm{mm}$ thick, over-depleted germanium pn-junction are reported in Fig. 3.8. We assumed a donor concentration $N_D = 10^{11}\ cm^{-3}$ and $E_{min} = 0.8\ E_{max}$.

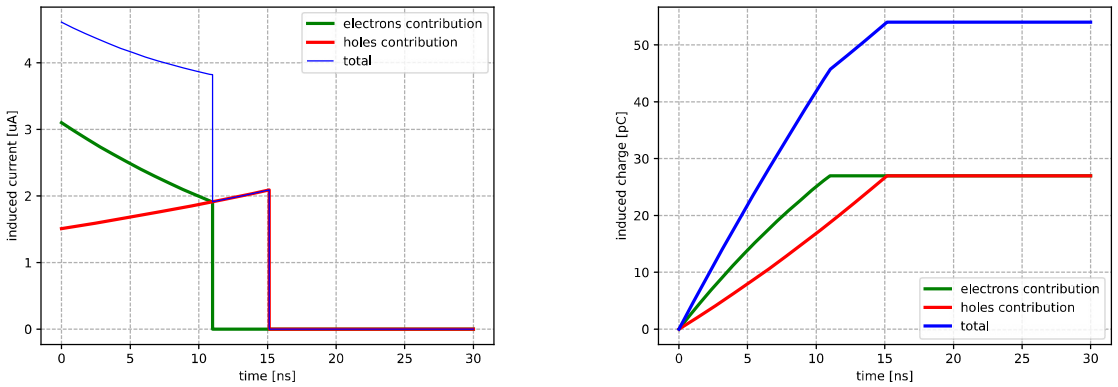

(a) Current induced by the point-like charge in a pn-junction

(b) Charge induced by the point-like charge in a pn-junction

Figure 3.8: Simulation of the induced current and charge generated by a $1\,\mathrm{MeV}$ photon interacting at the midpoint of an over-depleted pn-junction $10\,\mathrm{mm}$ thick.

3.2 The Charge Sensitive Preamplifier

A charge-sensitive preamplifier (fig. 3.9) is a negative feedback amplifier with capacitive feedback. The feedback capacitance, C_f, defines the closed-loop gain of the circuit, which determines the relationship between the output signal amplitude and the input current induced by the charge generated within the detector. The detector is schematically modeled by a current generator and a capacitor, C_{det}, representing the intrinsic capacitance of the depleted detector volume. A high-value feedback resistor R_f is also included to establish the correct DC operating point of the amplifier. Moreover, it prevents continuous saturation of the preamplifier by enabling the gradual discharge of the feedback capacitor, thereby ensuring stable long-term operation.

As previously described, the induced current signal i_{in}, whose time integral corresponds to the charge Q produced by the incident radiation interaction, can be approximated as a delta-like pulse:

$$i_{in}(t) = Q\delta(t) \tag{3.37}$$

Assuming an ideal amplifier with infinite gain and no bandwidth limitation, the feedback impedance assumes the form:

$$Z_f = \frac{R_f}{1 + sC_fR_f} \tag{3.38}$$

where s is the Laplace complex frequency. Consequently, in the Laplace domain, the voltage signal at the output of the charge preamplifier is given by:

$$v_{out}(s) = -i_{in}(s)Z_f = -Q\frac{R_f}{1 + sC_fR_f} \tag{3.39}$$

By applying the inverse Laplace transform to this expression, the time-domain representation of the signal is obtained:

$$v_{out}(t) = -\frac{Q}{C_f}\exp(-\frac{t}{\tau_f})\theta(t) \tag{3.40}$$

with $\theta(t)$ the Heaviside step function and $\tau_f = C_fR_f$ the preamplifier time constant.